Cell Reports
Physical Science

CellPress
OPEN ACCESS

Article

Evidence of hydrogen content and monovalent Ni oxidation state in non-superconducting bulk anchored infinite-layer nickelates

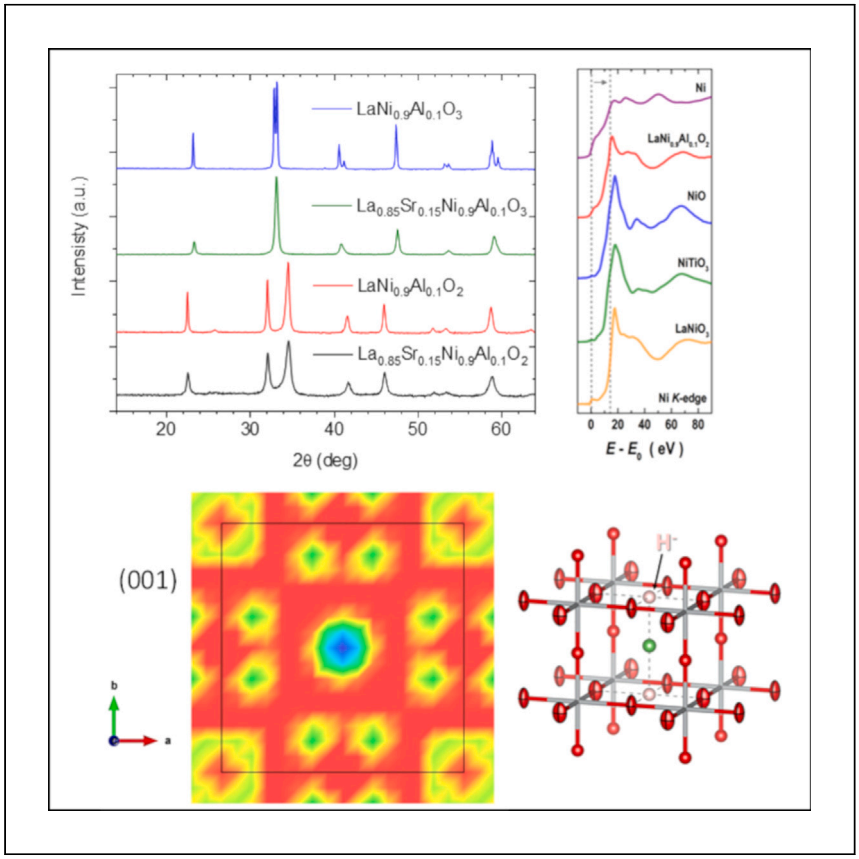

Gainza et al. report new findings on infinite-layer nickelates, a family of nickel-based high-temperature superconductors, similar to high-T_c cuprates. The bulk-powder laminar $LaNi_{0.9}Al_{0.1}O_{2.1}$ has hydrogen at the centers of the Ni–O squares, with spectroscopic evidence for a rare Ni^+ oxidation state.

Javier Gainza, Carlos A. López, Federico Serrano-Sánchez, ..., María T. Fernández-Díaz, José Luis Martínez, José Antonio Alonso

j.gainza@csic.es (J.G.)
nmnemes@ucm.es (N.M.N.)
ja.alonso@icmm.csic.es (J.A.A.)

Highlights

Anchored laminar infinite-layer nickelate $LaNi_{0.9}Al_{0.1}O_{2.1}$ prepared as bulk powder

Neutron diffraction locates hydrogen at the centers of the Ni–O squares

Spectroscopic evidence for rare Ni^+ oxidation state

Gainza et al., Cell Reports Physical Science 4, 101724
December 20, 2023
https://doi.org/10.1016/j.xcrp.2023.101724

Cell Reports
Physical Science

CellPress
OPEN ACCESS

Article

Evidence of hydrogen content and monovalent Ni oxidation state in non-superconducting bulk anchored infinite-layer nickelates

Javier Gainza,[1,*] Carlos A. López,[2] Federico Serrano-Sánchez,[1] João Elias F.S. Rodrigues,[3] Angelika D. Rosa,[3] María Isabel Sobrados,[1] Norbert M. Nemes,[1,4,*] Neven Biskup,[4] María T. Fernández-Díaz,[5] José Luis Martínez,[1] and José Antonio Alonso[1,6,*]

SUMMARY

Since superconductivity was first reported in nickelate thin films, many studies have been published about this family of materials, and different hypotheses have been proposed for explaining the mechanisms and structural dependence. Here, we report the synthesis of anchored infinite-layer $LaNi_{0.9}Al_{0.1}O_{2.1}$ and its hole-doped derivatives by topotactic reduction from $La_{1-x}Sr_xNi_{0.9}Al_{0.1}O_3$ rhombohedral perovskites. $LaNiO_2$ derivatives constitute a new family of high-temperature superconductors, with the same structure as high-T_c cuprates but based on nickel, only showing superconductivity in thin films for now. We describe a strategy to stabilize $LaNiO_2$ derivatives in bulk: the presence of Al at the octahedral sites helps to stabilize/anchor the infinite-layer structure. The reasons for the bulk being non-superconductors are hotly debated in the literature. An important question is whether there is some hydrogen incorporated into the structure during the reduction process from $LaNiO_3$ to $LaNiO_2$, predicted theoretically but not reported experimentally. Our neutron powder diffraction data show that, indeed, hydrogen occupies the centers of the Ni–O squares, and spectroscopic evidence from EELS and XAS suggests that Ni is reduced to the Ni^+ oxidation state, consistent with the crystallochemical data.

INTRODUCTION

The discovery of unconventional superconductivity in the $Ba_xLa_{5-x}Cu_5O_{5(3-y)}$ system by Bednorz and Müller[1] more than 35 years ago revolutionized the field of condensed matter physics and, even today, remains one of the most important and challenging problems in the field. A promising approach to solve these long-standing issues involves comparing cuprate superconductors with similar compounds and determining which features of the cuprates are crucial for the emergence of superconductivity. Although high-T_c superconductivity is found in cuprates with different crystalline structures,[2] the best candidates for mimicking their superconducting properties must show a quasi-two-dimensional structure, with a weak interplane coupling, and a key structural unit equivalent to the [CuO_2] plane present in the original compound.[3] The infinite-layer nickelates fulfill all these requirements, and they were already proposed by V. Anisimov et al. in 1999 as analogs of superconducting cuprates.[4]

Despite all the extensive research on nickelates carried out during the last decades,[5–15] it was only in 2019 that D. Li et al. reported superconductivity in $Nd_{0.8}Sr_{0.2}NiO_2$ thin

[1]Instituto de Ciencia de Materiales de Madrid, CSIC, Cantoblanco, 28049 Madrid, Spain

[2]INTEQUI, (UNSL-CONICET) and Facultad de Química, Bioquímica y Farmacia, UNSL, Almirante Brown 1455, San Luis 5700, Argentina

[3]European Synchrotron Radiation Facility (ESRF), 71 Avenue des Martyrs, 38000 Grenoble, France

[4]Departamento de Física de Materiales & Instituto Pluridisciplinar, Universidad Complutense de Madrid, 28040 Madrid, Spain

[5]Institut Laue-Langevin, 38000 Grenoble Cedex, France

[6]Lead contact

*Correspondence: j.gainza@csic.es (J.G.), nmnemes@ucm.es (N.M.N.), ja.alonso@icmm.csic.es (J.A.A.)

https://doi.org/10.1016/j.xcrp.2023.101724

films,[16] with further reports of superconductivity in different nickel compositions being published from that time onward.[17–23] The infinite-layer nickelate $RNiO_2$ (R = rare-earth elements) possesses an identical crystal structure to the cuprate parent compound $CaCuO_2$. Besides, although there exist several differences between the two transition metal ions,[24] the electronic configuration of Ni^+ in layered nickelates resembles those of Cu^{2+} in cuprates,[25,26] with a nominal d^9 configuration, where their antibonding e_g shells are partially filled with three electrons, with a single hole in the $3d_{x^2-y^2}$ orbital.

Since superconductivity was first reported in nickelate thin films in 2019, many studies have been published about this family of materials,[27–37] and different hypotheses have been proposed for explaining the mechanisms and their absence in the bulk form. Presently, the most supported hypothesis relies on the potential effect of interstitial hydrogen on the superconducting properties of these nickelates.[38–42] According to X. Ding et al.,[42] the reduction process of $RNiO_3$ leading to $RNiO_2$ using CaH_2 leads to the incorporation of hydrogen in the apical oxygen sites, which modifies the electronic structure of the H-doped nickelate to a one more two-dimensional-like—more precisely, annihilating the itinerant interstitial *s* orbitals, thus blocking the interlayer hopping.[42] The amount of hydrogen intercalated seems to increase with the reduction time[40] at the same time that a very narrow superconducting window appears for a particular H-doping interval.[42] For the case of infinite-layer $LaNiO_2$, theoretical work by L. Si et al.[38] found H intercalation to be energetically favorable for this compound, changing the electronic structure from being similar to that of doped cuprates toward a two-orbital Mott insulator. P. Puphal et al.[40] successfully synthesized a bulk infinite-layer $LaNiO_2$, showing no superconductivity. Furthermore, using neutron powder diffraction (NPD), they concluded that the presence of intercalated hydrogen is unlikely in their powder samples and that it may be located in grain boundaries or secondary-phase precipitates.

Apart from all the prior considerations, it is important to mention that the synthesis of the reduced phase itself, $RNiO_2$, is not a simple task due to the difficulty of stabilizing the Ni^+ oxidation state without decomposing the bulk sample.[43–46] Besides, to synthesize the starting compound, $RNiO_3$, high temperatures and high oxygen pressures are required,[13] relatively extreme conditions that are not available in all laboratories. Although there have been several reports on the synthesis of bulk nickelates in the past years,[32,37,46,47] none of them have been reported to be superconducting to date.

In this work, with the idea of shedding some light on the behavior of rare-earth infinite-layer nickelates, as well as exploring their possible superconducting properties in bulk, we report the synthesis of $La_{1-x}Sr_xNi_{0.9}Al_{0.1}O_2$ anchored infinite-layer compounds in powder form (bulk). Using a citrate-nitrate route and substituting some of the nickel with aluminum to help hold the layers together,[48] we have synthesized anchored infinite-layer nickelates with a Ni^+ oxidation state and Sr doping. We emphasize the necessity of the partial Al substitution in the perovskite to facilitate the following reduction process without decomposition and metallic nickel formation. Although the x = 0.15 compound shows the most promising properties at first, superconductivity is not observed in any of the samples. By means of Fourier analysis from NPD data, we have detected a negative nuclear density compatible with the presence of hydrogen within the layers, confirming the trapped hydrogen hypothesis in the bulk but without revealing superconductivity, perhaps due to an excess of the hydrogen amount; furthermore, thermogravimetry coupled to mass spectroscopy detected H_2 gas evolution above 200°C, and infrared spectroscopy and ^1H nuclear magnetic resonance evidenced features consistent with metal hydrides. We have also carried out a thorough structural analysis based on NPD and synchrotron X-ray

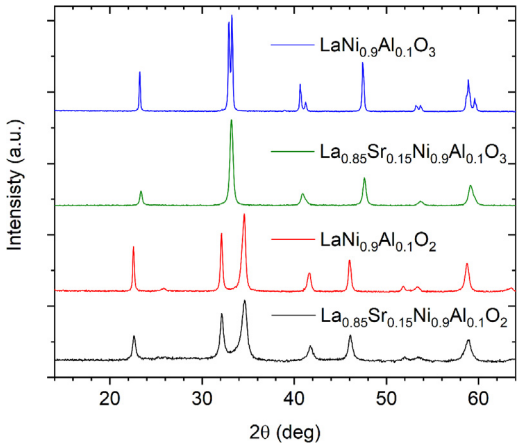

Figure 1. X-ray diffraction patterns of perovskite and anchored infinite-layer nickelates

$La_{1-x}Sr_xNi_{0.9}Al_{0.1}O_3$ (x = 0 in blue, x = 0.15 in green) and $La_{1-x}Sr_xNi_{0.9}Al_{0.1}O_2$ (x = 0 in red, x = 0.15 in black). See also Figures S1 and S3.

diffraction (SXRD) data, as well as a complete magnetic characterization to unveil the relevant features responsible for the absence of superconductivity in these bulk samples. This is complemented with spectroscopic measurements, X-ray absorption spectroscopy (XAS), and electron energy-loss spectroscopy (EELS) to provide evidence of the presence of monovalent nickel in the infinite-layer frameworks.

RESULTS

Initial characterization

Well-crystallized samples of the oxidized $La_{1-x}Sr_xNi_{1-y}Al_yO_3$ (x = 0, 0.15; y = 0.1) and the corresponding reduced phases were obtained as black polycrystalline powders. The laboratory XRD patterns are shown in Figure 1. The perovskite oxidized phases were indexed with rhombohedral symmetry (analogous to $LaNiO_3$; space group $R\bar{3}c$) as described in a previous report.[48] The unit-cell parameters were a = 5.448(7) Å and c = 13.1511(18) Å for $LaNi_{0.9}Al_{0.1}O_3$ and a = 5.4278(7) Å and c = 13.1979(26) Å for $La_{0.85}Sr_{0.15}Ni_{0.9}Al_{0.1}O_3$, determined by Rietveld refinement from laboratory XRD data. The Sr^{2+} incorporation at the La^{3+} sites induces a significant variation of the unit-cell size, as a result of the hole-doping effect that increases the Ni oxidation state, combined with the larger ionic size of Sr^{2+} vs. La^{3+}. The reduced phases, with nominal composition $LaNi_{0.9}Al_{0.1}O_2$ and $La_{0.85}Sr_{0.15}Ni_{0.9}Al_{0.1}O_2$, are tetragonal, space group $P4/mmm$, with unit-cell parameters a = 3.9484(7) Å and c = 3.4562(7) Å and a = 3.9414(11) Å and c = 3.450(12) Å, respectively. Detailed structural analysis of the oxidized $LaNi_{0.9}Al_{0.1}O_3$ is included in the supplemental experimental procedures, Figures S1 and S2, and Tables S1 and S2 and for $La_{0.85}Sr_{0.15}Ni_{0.9}Al_{0.1}O_3$ in Figure S3 and Table S3.

SXRD analyses

The better crystallinity of the $LaNi_{0.9}Al_{0.1}O_2$ as compared to the Sr-doped phase enabled a comprehensive analysis of the SXRD patterns and determined the crystal structure as an anchored infinite-layer (IL) material. The microstrain effects observed and modeled in both NPD and SXRD indicate, overall, the lack of very high crystallinity. It is confirmed that it crystallizes in the tetragonal $P4/mmm$ space group (#123), consistent with the finding reported by Hayward et al.[45] As mentioned in the introduction, in the IL $LaNiO_2$ derivatives from the perovskite structure, there is a topotactic oxide de-intercalation affecting the axial oxygen atoms of the $[NiO_6]$ octahedra of the oxidized perovskite phase, thus resulting in layers of $[NiO_4]$ square planes connected by corners and separated by lanthanum cations. In the current phase, the nickel and aluminum cations are randomly distributed at

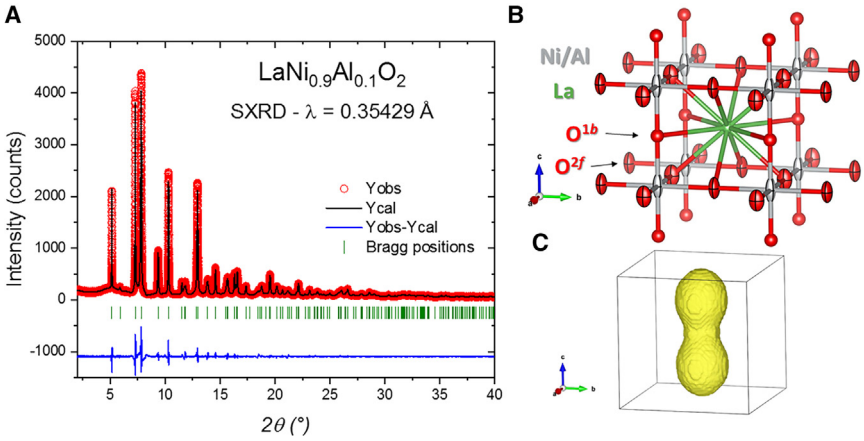

Figure 2. Structure of anchored infinite-layer nickelate from SXRD

(A) Rietveld refinement of $LaNi_{0.9}Al_{0.1}O_2$ SXRD pattern at room temperature.

(B) Schematic view of crystal structure representation.

(C) Shape of microstrain effects.

See also Figure S4.

the 1*a* (0,0,0) Wyckoff site, while the lanthanum are located at the 1*d* (0.5,0.5,0.5) site. The oxygen anions occupy the 2*f* (0.5,0,0) site. It is worth noting that the 1*b* site, which would complete the nominal ABO_3 perovskite-type structure, remains partially unoccupied since the axial oxygen atoms directly linked to Al^{3+} ions are not eliminated in the reduction process: the presence of $[AlO_6]$ bridges distributed at random link together adjacent layers, thus stabilizing the IL structure.

The SXRD pattern was successfully indexed using this model; however, several peak discrepancies were observed due to anisotropic broadening effects. Upon closer inspection, it was noted that the family of (*0*, *0*, *n*) planes exhibited greater broadening compared to the (*n*, *0*, *0*) planes. To investigate this effect, various combinations of anisotropic size and/or strain models were tested in an effort to improve the profile matching of the pattern. A good agreement was achieved by considering an isotropic size and anisotropic strain broadening in the 4/*mmm* Laue class. The obtained strain effects are greater along the c axis than in the ab plane, which can be related to the layered nature of this phase. After achieving a satisfactory fitting of the peak shape, specific crystallographic characteristics such as the anisotropic displacement factors were refined. Subsequently, the presence of the mentioned axial oxygens at the 1*b* (0,0,0.5) Wyckoff site was investigated, resulting in an occupancy of 11.5%, in close agreement with the Al doping level of 10%. Figure 2A illustrates the good agreement reached for the SXRD pattern, and Table 1 lists the main crystallographic data. Figure 2B shows a schematic view of crystal structure and the shape results of the anisotropic strain effect.

NPD analyses

A remarkable aspect of these IL compounds lies in the possible presence of hydrides within their structures. Previous studies have provided theoretical support[40,41,49,50] for the plausible presence of hydrides and their impact on the properties. However, the specific location of the hydrides is still not fully understood. According to theoretical predictions, the H^- ions can be located either on the vacant apical oxygen sites with Wyckoff position (1*b*) or on interstitial positions between the rare-earth ions with Wyckoff positions (2*e*) and (1*c*).[51] Nonetheless, recent neutron diffraction

Table 1. Main crystallographic results of $LaNi_{0.9}Al_{0.1}O_2$ from SXRD data

Fractional atomic coordinates and isotropic or equivalent isotropic displacement parameters (Å^2)					
	x	y	z	U_{iso}*/U_{eq} (Å^2)	Occ. (<1)
La	0.50000	0.50000	0.50000	0.01076(4)*	–
Ni/Al	0.00000	0.00000	0.00000	0.0184(2)	0.90/0.1
O1	0.50000	0.00000	0.00000	0.0187(9)	–
O2	0.00000	0.00000	0.50000	0.00633*	0.115(2)

	*U*11	*U*22	*U*33	*U*12	*U*13	*U*23
Atomic displacement parameters (Å^2)						
Ni/Al	0.0059(2)	0.0059(2)	0.0433(4)	0.00000	0.00000	0.00000
O1	0.0101(8)	0.0144(8)	0.032(1)	0.00000	0.00000	0.00000

Space group: *P*4/*mmm*. Unit-cell parameters: a = 3.94793(1) Å, c = 3.45810(2) Å, and V = 53.90(1) Å^3. Reliability factor: R_p = 5.08%, R_{wp} = 6.50%, R_{exp} = 2.29%, R_{Bragg} = 1.90%, χ^2 = 8.95.

studies did not find solid evidence of the presence of ordered H^- ions in the crystal structure.[40]

NPD data were collected for both oxidized ($LaNi_{0.9}Al_{0.1}O_3$ and $La_{0.85}Sr_{0.15}Ni_{0.9}Al_{0.1}O_3$) and corresponding reduced samples (Figure S4). The crystal structures of the oxidized nickelates were refined in the $R\bar{3}c$ conventional model (isostructural to $LaNiO_3$), and the crystallographic parameters and Rietveld plots are included in Table S1 and S2 and Figures S1 and S2, respectively, thus assessing the quality of the bulk precursors utilized in the reduction to the IL compounds.

The good crystallinity of our reduced $LaNi_{0.9}Al_{0.1}O_2$ specimen allowed us to unveil additional information from neutron diffraction, based on the structural model previously described from SXRD data. Firstly, the crystallographic structure (Table 1) was kept fixed, while both instrumental and microstructural parameters were refined. The microstructure was accurately modeled using the same criteria employed in the analysis of synchrotron data. Afterward, difference Fourier maps (DFMs) were calculated to identify negative densities and provide evidence of the presence of hydrogen atoms. Figure 3 displays the resulting DFMs, where negative nuclear densities are observed in the *1c* sites (at the midpoint between La atoms along the c axis). The two-dimensional plots (Figure 3B) further confirm this observation and provide evidence on the absence of H^- in alternative locations.

Based on these nuclear density observations, a hydrogen atom was added in the 1*c* Wyckoff site, and its occupancy parameter was refined. The results indicate that the hydrogen occupancy at the 1*c* (0.5, 0.5, 0) site is approximately 6.9%. This led to a good fit of the neutron pattern, as shown in Figure 4A. A schematic representation of the obtained structure is illustrated in Figure 4B, and the crystallographic data are listed in Table 2. Based on these findings, it is possible to propose the crystallographic formula $LaNi_{0.9}Al_{0.1}O_{2.11}H_{0.07}$ for the obtained IL phase. Unfortunately, the much poorer quality of the NPD pattern for the hole-doped $La_{0.85}Sr_{0.15}Ni_{0.9}Al_{0.1}O_2$ prevented the refinement of its crystal structure (Figure S5; Table S4). The thermal evolution of the structural parameters of $LaNi_{0.9}Al_{0.1}O_2$ is analyzed in Figures S6 and S7 and Table S5. Direct evidence of hydrogen content was provided by mass spectroscopy of the evolved gases during thermogravimetry analysis of the sample, as shown in Figures S8 and S9. Further evidence of hydrogen content was gathered using Fourier transform infrared (FTIR) and nuclear magnetic resonance (NMR) spectroscopies that detect features consistent with, but not identical to, metal hydrides, as described in the supplemental information and Figures S10 and S11.

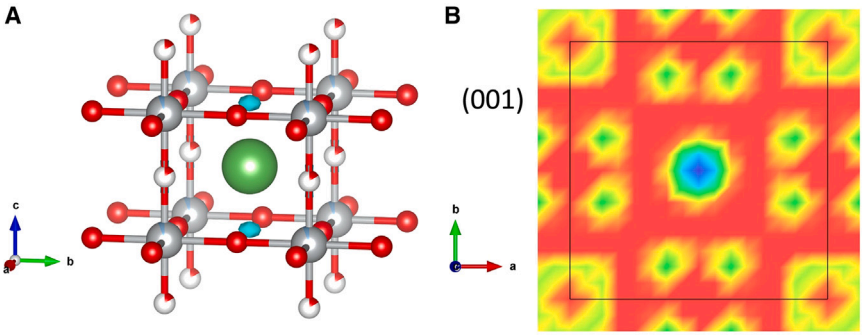

Figure 3. Locating hydrogen with neutron diffraction in $LaNi_{0.9}Al_{0.1}O_2$

(A) Three-dimensional plots of difference Fourier maps of NPD together with the crystal structure. The blue regions indicate the zones with negative density (in terms of scattering density).

(B) Two-dimensional plot of Fourier maps in the (001) plane.

Magnetic properties

The dependence on temperature of the magnetic susceptibility for $LaNi_{0.9}Al_{0.1}O_2$ (Figure 5A) indicates neither a superconducting behavior nor a simple Curie-Weiss paramagnetic response. For the hole-doped compound ($La_{0.85}Sr_{0.15}Ni_{0.9}Al_{0.1}O_2$), the magnetic susceptibility is much lower (almost two orders of magnitude), probably indicating an increase in the metallicity, with respect to the previous compound but does not reach a superconducting state. The temperature response in both cases is rather featureless.

At low temperature, the magnetic field dependence of the magnetization in Figure 5B shows a ferromagnetic (or superparamagnetic) sigmoid behavior for $LaNi_{0.9}Al_{0.1}O_2$, probably related to small particles of Ni segregated in the reduction process (not detected by diffraction methods). In the case of $La_{0.85}Sr_{0.15}Ni_{0.9}Al_{0.1}O_2$, a similar behavior is observed. This indicates that, probably, the reduction procedure is analogous in both cases, with no significant influence on the level of Sr (carrier) doping.

EELS

Figure 6 shows the scanning transmission electron microscopy images and spectrometry of $LaNi_{0.9}Al_{0.1}O_2$. The high-angle annual dark field (HAADF) image in Figure 6A shows the atomic structure of $LaNi_{0.9}Al_{0.1}O_2$ oriented along the [001] zone axis. Larger/brighter atoms are the heavier lanthanum atoms, and smaller/dimmer atoms are nickel/aluminum atoms. Oxygen atoms cannot be observed in this HAADF image. Figure 6B shows the crystal model based on the neutron diffraction data. Figure 6C is the comparison of EELSs of the reduced $LaNi_{0.9}Al_{0.1}O_2$ (red) and the oxidized $LaNi_{0.9}Al_{0.1}O_3$ (blue). The dispersion of $\Delta E = 0.1$ eV permits the focus on the La $M_{4,5}$ and Ni $L_{2,3}$ edges. Figure 6D is the same comparison but with the dispersion of $\Delta E = 0.25$ eV, enabling also the detection of the oxygen K edge. The reduced material has a much weaker oxygen edge—the E = 526 eV pre-peak is completely absent, and the second peak at E = 540 eV is much smaller. These are the signatures of strong oxygen deficiency and have already been observed in IL nickelates.[52] The analysis of the nickel $L_{2,3}$ edge yields the same conclusion. The lanthanum M_4 edge overlaps with the nickel L_3 edge at 855 eV and thus hinders straightforward identification of the nickel oxidation state. However, the Ni L_2 edge in $LaNi_{0.9}Al_{0.1}O_3$ (nominally Ni^{3+}) is clearly higher than in $LaNi_{0.9}Al_{0.1}O_2$ (nominally Ni^{+}). The smaller Ni L_2 edge in the reduced material is visible in both Figures 6C and 6D. This resembles the case of a related pair of compounds studied for the

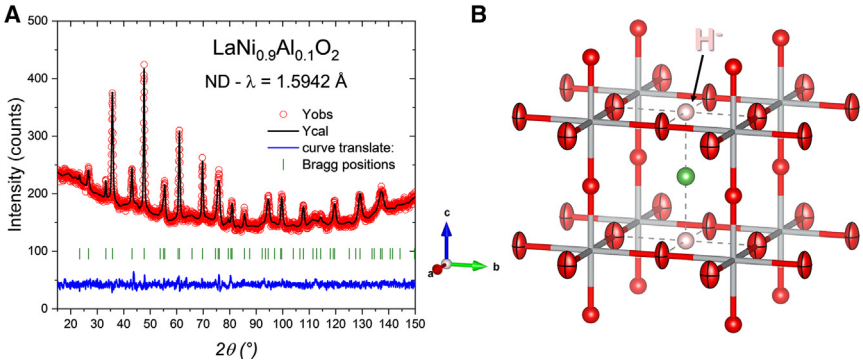

Figure 4. Crystal structure representation of hydrogen containing anchored infinite-layer nickelate from NPD

(A) Rietveld refinement of $LaNi_{0.9}Al_{0.1}O_2$ NPD pattern at room temperature.

(B) Schematic view of crystal structure.

See also Figure S5.

sake of comparison: $PrNiO_3$ (Ni^{3+}) and $PrNi_{0.9}Al_{0.1}O_2$ (Ni^{+}). Praseodymium has the advantage that the Pr $M_{4,5}$ edge lies at E = 931 eV and does not overlap with the Ni $L_{2,3}$ edge (shown in Figure S12). Reduced (Ni^{+}) praseodymium nickelate has a weaker Ni L_2 edge compared to the Ni^{3+} compound, as observed in the case of lanthanum nickelate. This is the consequence of different L_{23} ratios between the nickel L_3 and L_2 edges, a well-known measure of the oxidation state in transition metals.[53,54] We estimated this ratio using the ratio of the second derivative of each EELS edge[55] and have found values of L_{23} = 2.5 ± 0.2 for the Ni^{3+} ion and L_{23} = 3.5 ± 0.2 for the Ni^{+} ion. Based on this comparison, we argue that the slightly weaker Ni L_2 edge in Figures 6C and 6D is a signal of the Ni^{+} oxidation state.

X-ray absorption results

The Ni *K*-edge X-ray absorption spectra of $LaNi_{0.9}Al_{0.1}O_2$ are compared to those of reference compounds in Figure 7, such as Ni foil (Ni^0), NiO (Ni^{2+}), $NiTiO_3$ (Ni^{2+}), and $LaNiO_3$ (Ni^{3+}). In Figure 7A, the X-ray absorption near-edge structure (XANES) region is highlighted. We observe a clear progressive blueshift of the edge region (delineated by two dashed lines in Figure 7A) from 8,333.0 (Ni) to 8,341.9 ($LaNiO_3$) eV. This shift is a strong indicator for the Ni valence state variation from 0 to 3+, respectively. For $LaNi_{0.9}Al_{0.1}O_2$, the edge position is around 8,336.6 eV in between Ni and NiO, denoting that the Ni valence state in $LaNi_{0.9}Al_{0.1}O_2$ is 1+.

Table 2. Main crystallographic results of $LaNi_{0.9}Al_{0.1}O_2$ from NPD data

Fractional atomic coordinates and isotropic or equivalent isotropic displacement parameters (Å^2)					
	x	y	z	U_{iso}*/U_{eq}	Occ. (<1)
La	0.50000	0.50000	0.50000	0.014(1)*	–
Ni/Al	0.00000	0.00000	0.00000	0.017(2)	0.90/0.1
O1	0.50000	0.00000	0.00000	0.013(2)	–
O2	0.00000	0.00000	0.50000	0.00633*	0.115
H	0.50000	0.50000	0.00000	0.01900*	0.069(8)

	*U*11	*U*22	*U*33	*U*12	*U*13	*U*23
Atomic displacement parameters (Å^2)						
Ni/Al	0.0009(8)	0.0009(8)	0.049(3)	0.00000	0.00000	0.00000
O1	0.0070(13)	0.0109(13)	0.020(2)	0.00000	0.00000	0.00000

Space group: *P*4/*mmm*. Unit-cell parameters: a = 3.9483(1) Å, c = 3.4587(3) Å, and *V* = 53.92(1) Å^3. Reliability factor: R_p = 1.99%, R_{wp} = 2.58%, R_{exp} = 1.11%, R_{Bragg} = 3.41, χ^2 = 5.67. See also Table S5.

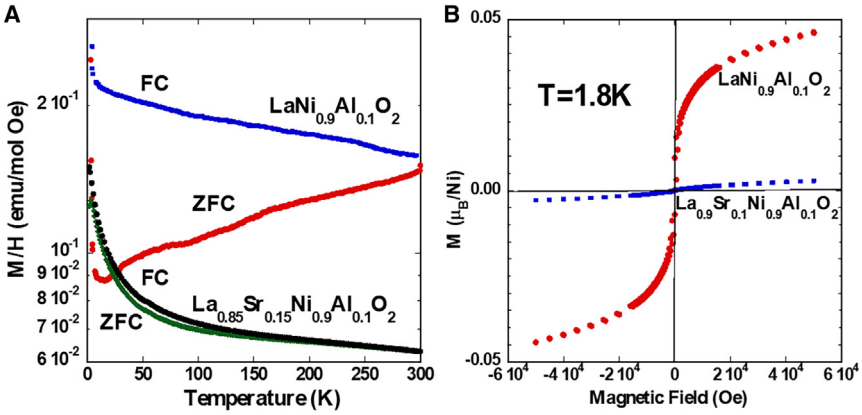

Figure 5. Magnetism of non-superconducting anchored infinite-layer nickelate

(A) Temperature dependence of the magnetic susceptibility under 10 or 100 Oe after zero-field cooling (ZFC) and field cooling (FC) conditions, for $LaNi_{0.9}Al_{0.1}O_2$ and $La_{0.85}Sr_{0.15}Ni_{0.9}Al_{0.1}O_2$. Note the logarithmic scale for the magnetic susceptibility.

(B) Magnetic field dependence of the magnetization at 1.8 K for $LaNi_{0.9}Al_{0.1}O_2$ and $La_{0.85}Sr_{0.15}Ni_{0.9}Al_{0.1}O_2$.

The individual XANES spectra also exhibit different features after the edge region, which reflects the strong sensitivity of XANES on the composition and local crystallographic symmetry of Ni in individual compounds. For instance, in NiO, $NiTiO_3$, and $LaNiO_3$, Ni is coordinated by 6 oxygen atoms in an octahedral environment. Spectra

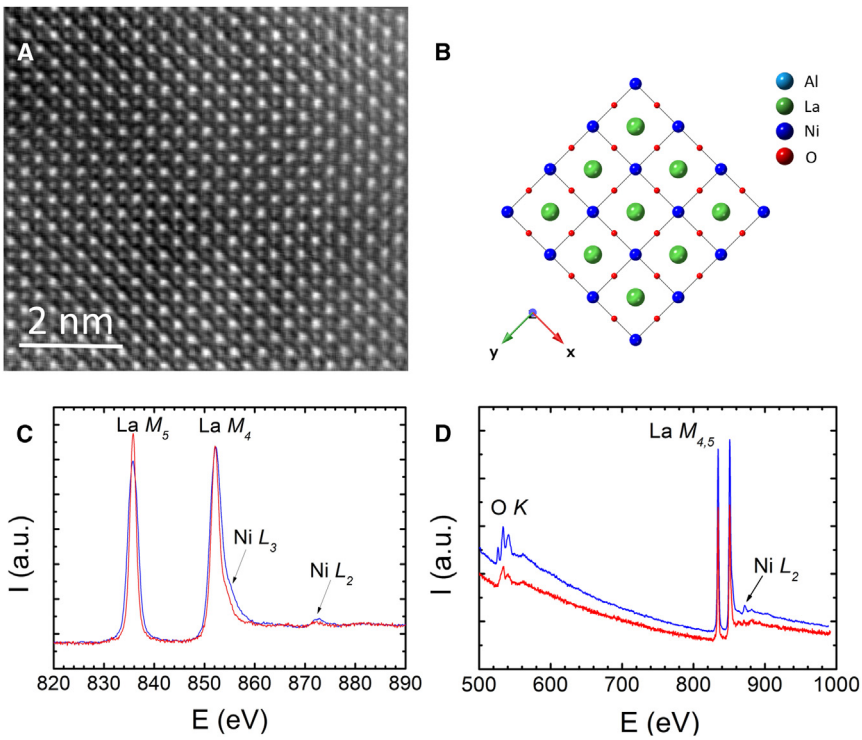

Figure 6. Spectroscopic evidence for Ni^+ oxidation state from electron microscopy

(A) Atomic-resolution HAADF image of $LaNi_{0.9}Al_{0.1}O_2$ crystal in [001] zone axis.

(B) Crystal model based on the neutron diffraction data.

(C) EELS spectra of $LaNi_{0.9}Al_{0.1}O_3$ (Ni^{3+}, blue line) and $LaNi_{0.9}Al_{0.1}O_2$ (Ni^+, red line) with $\Delta E = 0.1$ eV dispersion.

(D) The same as in (C) but with $\Delta E = 0.25$ eV dispersion.

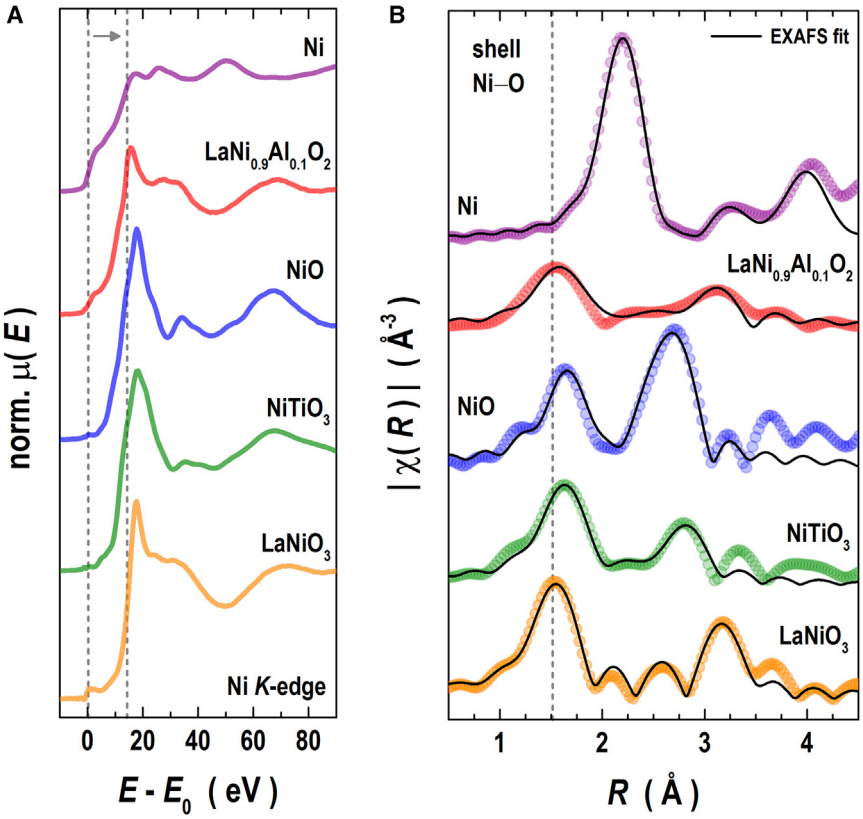

Figure 7. Spectroscopic evidence for Ni^{+} oxidation state from X-ray absorption

(A) Ni *K*-edge spectra collected at ambient conditions of the Ni foil (Ni^{0}), $LaNi_{0.9}Al_{0.1}O_2$ (Ni^{+}), NiO (Ni^{2+}), $NiTiO_3$ (Ni^{2+}), and $LaNiO_3$ (Ni^{3+}).

(B) Fourier moduli $|\chi(R)|$ for all the compounds, where open symbols are the experimental points and the black solid lines the best EXAFS fit obtained.

of these compounds show certain similarities, while differences among them can be explained by the different second-nearest neighbors, i.e., Ni, La, or Ti. The spectra of $LaNi_{0.9}Al_{0.1}O_2$ show strong differences to those described above and metallic Ni. This can be most likely related to the lower coordination number of Ni (4) in this structure and to the complex second-nearest-neighbor environment (Al, La, and potentially H).

In Figure 7B, the moduli of the Fourier transform $|\chi(R)|$ of the extended X-ray absorption fine structure (EXAFS) signal of the raw data (colored symbols) are compared to those obtained from EXAFS fitting (black lines). For the oxides, the moduli exhibit two peaks around 1.5 Å, followed by a second peak located at the interval 2.25–4 Å (not corrected by the photoelectron phase shift). Here, we will mainly discuss the local structure around the first shell composed by Ni and O atoms. Table 3 summarizes the average bond distance $R_{Ni–O}$, the coordination number, and the Debye-Waller factor for all the oxide compounds in Figure 7. We observe a shortening of the average Ni–O distance with increasing Ni valence state, as expected from theory from the bond valence sum.[56] For example, $R_{Ni–O}$ varies from 2.010(1) Å to 1.92(1) Å for a Ni valence from 1^{+} in $LaNi_{0.9}Al_{0.1}O_2$ to 3+ in $LaNiO_3$. Note that the Debye-Waller factor also decreased with decreasing bond distance (Table 3). In the case of $LaNi_{0.9}Al_{0.1}O_2$, the presence of H and vacancies on the apical oxygen sites may contribute to promote a structural disorder that raises the Debye-Waller factor in addition (σ^2 = 0.007(2) $Å^2$). In summary,

Table 3. Structural parameters refined from the $LaNi_{0.9}Al_{0.1}O_2$ EXAFS data for the first-shell Ni-O, such that R_{Ni-O} is the average bond distance, N_{Ni-O} the coordination number, and σ^2 the Debye-Waller factor

Compound	Edge pos. (eV)	R_{Ni-O} (Å)	N_{Ni-O}	σ^2 (Å^2)	*R* factor
Ni foil	8,333.0	–	–	–	–
$LaNi_{0.9}Al_{0.1}O_2$	8,336.6	2.010(1)	4	0.007(2)	0.1195
NiO	8,339.1	2.093(7)	6	0.005(2)	0.0517
$NiTiO_3$	8,339.3	2.050(1)	3+3	0.003(1)	0.0327
$LaNiO_3$	8,341.9	1.92(1)	6	0.0011(8)	0.0302

The edge position obtained from XANES is also reported. See also Table S6.

observations in both XANES and EXAFS suggest a Ni oxidation state of 1+ in $LaNi_{0.9}Al_{0.1}O_2$ and confirm a complex chemical environment.

DISCUSSION

We have demonstrated that the stabilization of Ni^+ in defect perovskites $La(Ni_{1-y}Al_y)O_{2+y}$ and the hole-doped counterparts is possible under mild reduction conditions with CaH_2, starting from suitable "oxidized" perovskites with $La_{1-x}Sr_xNi_{1-y}Al_yO_3$ stoichiometry. The reduced compounds could be indexed in a tetragonally distorted perovskite unit cell with a_0 edge dimensions. An NPD investigation, taking advantage of the higher sensitivity of neutrons to the oxygen and hydrogen atoms, were correctly refined on the basis of the structural model of the mentioned IL structure, typified by $SrCuO_2$.[57] The ideal ABO_2 IL structure can be derived from the ABO_3 network by removing all the axial oxygens, in such a way that B cations are coordinated to four oxygens, in square planar configuration. In the present structural refinement from NPD data, we assumed that Al cations, distributed at random in the Ni sublattice, keep the octahedral coordination even in the reduced phase, as illustrated in Figure 8.

Effectively, neutrons are able to detect the presence of some extra oxygen atoms at the axial positions, in the adequate proportion (about 0.1 atoms per formula unit) to complete the Al octahedral coordination. Therefore, Ni cations are in both square planar and square pyramidal coordination to oxygens, as shown in Figure 8. Note that the c axis is significantly shorter than the a axis, as observed in the tetragonal structure of $SrCuO_2$,[57] as a result of the absence of most of the axial oxygens. Also, a and c keep this relationship in the tetragonal lattice of pure $LaNiO_2$, as reported in the pioneering work by Crespin et al.[58] The presence of Al at the Ni

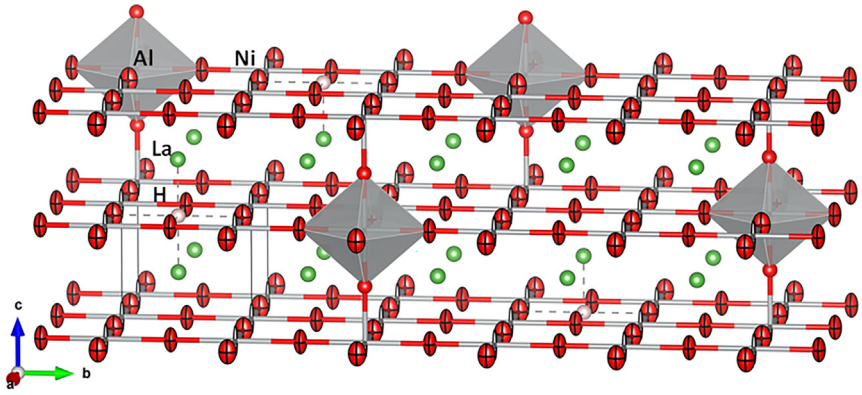

Figure 8. View of the $LaNi_{0.9}Al_{0.1}O_2$ crystal structure

The drawing shows the [AlO_6] octahedra bridging adjacent layers, the 4-or 5-fold coordination to oxygens of Ni^+ ions, and the statistical presence of H^- ions, at mid-distance between two La atoms.

sublattice is essential since the associated axial oxygens, acting as bridges between two adjacent layers, seem to favor the stability of the crystal structure.

The occurrence of Ni^{+} is doubly assessed; both EELS and XAS spectroscopic techniques unequivocally demonstrate the presence of this rare oxidation state for nickel. Magnetic measurements seem to indicate, in the reduced samples, the segregation of some Ni metal. In any case, segregated Ni has not been identified by SXRD or even by neutron diffraction (this element exhibiting one of the largest scattering lengths), perhaps by its occurrence in nanoparticulate form, below the detection limit by scattering techniques. In any event, the magnetic susceptibility does not exhibit any hints for superconductivity, either in the La specimen or in the hole-doped ($La_{0.85}Sr_{0.15}Ni_{0.9}Al_{0.1}O_2$) counterpart.

Finally, perhaps the most striking feature of these IL nickelates is the presence of some H^{-} ions, statistically distributed in the tetragonal unit cell, in a non-negligible proportion of about 0.07 atoms per formula unit, as determined from NPD data. This is the first report, to our knowledge, of the existence of H atoms within the crystal structure of an IL compound, in between the square planar [NiO_4] units. As discussed above, this has been a topic of debate,[38,40,42,52,53,59] as theoretical work[38] found H intercalation to be energetically favorable for this compound, leading to important changes in the electronic structure. Previous works using NPD concluded that the presence of intercalated hydrogen is unlikely in their powder samples and that it may be located in grain boundaries or secondary-phase precipitates. In our case, as described before, DFMs from NPD data indeed exhibit a negative scattering density located at a mid-distance between La ions, compatible with the presence of hydrogen within the layers, confirming the trapped hydrogen hypothesis in bulk materials. The absence of superconductivity in our specimens, even in the hole-doped material with stoichiometry $La_{0.85}Sr_{0.15}Ni_{0.9}Al_{0.1}O_2$, could well be related to the H inclusion, inherent to the synthesis procedure, although other hypotheses should not be discarded.

EXPERIMENTAL PROCEDURES

Resource availability

Lead contact

Further information and requests for resources and reagents should be directed to and will be fulfilled by the lead contact, Jose Antonio Alonso (ja.alonso@icmm.csic.es).

Materials availability

This study did not generate new unique reagents. Oxidized and reduced nickelates can be obtained upon request to the lead contact.

Data and code availability

The authors declare that data supporting the findings of this work are available within the article and the supplemental information. Any other data are available from the lead contact upon reasonable request.

Reagents

The following reagents were used as obtained, unless otherwise noted, in nominal stoichiometric amounts: La_2O_3 (99.9%, REO, Alfa Aesar), $SrCO_3$ (Merck), $Al(NO_3)_3 \cdot 9H_2O$ (>98.5%, Merck), and $Ni(NO_3)_2 \cdot 6H_2O$ (≥98.5%, Sigma-Aldrich).

Synthesis protocol of precursor perovskite

$La_{1-x}Sr_xNi_{1-y}Al_yO_3$ nickelates were prepared in polycrystalline form using a citrate-nitrate route. The reagents, La_2O_3, $SrCO_3$, $Al(NO_3)_3 \cdot 9H_2O$, and $Ni(NO_3)_2 \cdot 6H_2O$ were diluted in citric acid with some additional droplets of nitric acid to facilitate dissolution of the reagents. The mixture of citrate and nitrate solutions was slowly evaporated in a hot plate, leading to organic resins, which were dried and decomposed by slowly heating up to 600°C in air for 12 h and, afterward, were heated up to 800°C in air for 2 h, producing highly reactive precursor materials. The precursor powders were treated at 900°C under 200 bar O_2 pressure for 12 h in a Morris Research furnace. Finally, the samples were slowly cooled down (2°C/min) to room temperature to obtain the oxidized $La_{1-x}Sr_xNi_{1-y}Al_yO_3$ nickelates in a polycrystalline (powder) form.

Reduction protocol

For the chemical reduction process, the nickelate powder was ground and mixed with CaH_2, sealed under vacuum in a Pyrex tube, and placed in a furnace. The sample was heated for 0.5 h up to ~280°C, held for 6 h, and then cooled down to room temperature. At this point, and before breaking the Pyrex tube, the presence of metallic Ni can be checked by using a magnet close to the powder, so a rough estimation of the amount of Ni, if at all detectable, is obtained. Afterward, the Pyrex tube was opened, and the powder was washed with a 0.1 M solution of NH_4Cl and methanol (CH_3OH) for 1–2 h at room temperature and then was filtered to obtain the powder of the IL nickelates.

Neutron and XRD measurements

The powders of both oxidized and reduced compounds were analyzed by laboratory XRD in a Bruker D8 Advance, with Cu Kα radiation. Some selected samples were studied with NPD in the high-resolution D2B diffractometer at the Institut Laue-Langevin (ILL) in Grenoble, France. NPD patterns for four selected samples with nominal compositions $LaNi_{0.9}Al_{0.1}O_3$, $La_{0.85}Sr_{0.15}Ni_{0.9}Al_{0.1}O_3$, $LaNi_{0.9}Al_{0.1}O_2$, and $La_{0.85}Sr_{0.15}Ni_{0.9}Al_{0.1}O_2$ were collected at room temperature with a wavelength λ = 1.594 Å. The samples were contained in a cylindrical vanadium holder of 6 mm diameter. SXRD patterns were recorded at the ESRF beamline ID22 (Grenoble, France) operating at a wavelength of λ = 0.35429 Å (35 keV). The X-ray energy of 35 keV was chosen to minimize absorption effects. The samples were sealed in glass capillaries of 0.5 mm diameter and measured under rotation to minimize potential texture effects. The high-resolution powder diffraction patterns were collected over the range 1–40° (2θ) in continuous scanning mode for temperatures ranging from 6 to 300 K with a 15 min waiting time at each temperature step in order to guarantee an isothermal condition. SXRD patterns were retrieved following the processing method described by Fitch and Dejoie.[60,61]

XRD and NPD data analysis was performed by the Rietveld method with the FullProf program.[62,63] The refined parameters were the following: zero-point error, background coefficients, scale factor, asymmetry factors, lattice parameters, atomic fractional coordinates (x,y,z), and anisotropic thermal displacements.

Magnetometry

Magnetization measurements were performed in the temperature range from 1.8 to 300 K under an applied external magnetic field up to 7 T using a squid magnetometer (MPMS-3) from Quantum Design (San Diego, CA, USA).

STEM and EELS measurements

Scanning transmission electron microscopy (STEM) atomic-resolution images were taken in a JEOL ARM 200 electron microscope equipped with the aberration corrector. EELS spectrum images were taken with a Gatan "Quantum" detector.

X-ray absorption measurements

XAS measurements at the Ni *K*-edge (at 8.333 keV) and at room temperature were performed at the ESRF beamline BM23[64] using an unfocused beam collimated to 3 × 1 mm^2. A set of two parallel silicon mirrors inclined to 3 mrad and in fixed-exit geometry were employed for the harmonic rejection. For the measurements, we used sample pellets of 13 mm diameter that were made from finely ground powder mixed with appropriate proportions of cellulose in order to achieve an optimal absorption jump for X-ray absorption measurements at the Ni *K*-edge. The absorption coefficient, $\mu(E)$, of the sample was determined from beam intensity measurements before and after the measurements using two ionization chambers filled with appropriate gas mixtures to achieve 20% and 70% absorption of the X-ray beam photon flux, respectively. XAS data were acquired using an energy stepping of 0.25 eV in the XANES, which is most sensitive to the oxidation state and up to a *k*-range of 15 $Å^{-1}$ in the EXAFS region, which is sensitive to the average first-nearest-neighbor bond length and length distribution. Reference samples with well-known Ni oxidation states, including Ni foil (≥99.95%, Goodfellow), NiO (≥99.5%, Sigma-Aldrich), $NiTiO_3$ (in da Costa et al.[65]), and $LaNiO_3$ (in Martínez-Lope et al.[48]), were measured with the same parameters and served as standards for the analysis of the Ni oxidation state in $LaNi_{0.9}Al_{0.1}O_2$.

XAS data reduction was performed using the Athena software package and included pre-edge background subtraction, edge jump normalization, and the extraction of the EXAFS oscillations.[66] EXAFS fitting of the reduced data was conducted using the Artemis software.[66] Here, theoretical scattering paths were first calculated on the basis of a structural model using the *FEFF* multiple scattering path expansion. For these calculations, we used the structure data of reference samples and $LaNiO_2$ as reported from XRD measurements. The theoretical scattering paths are subsequently adjusted to the experimentally observed ones by adjusting structural parameters, including the average bond distance (R) and its distribution, here referred to as the Debye-Waller factor (σ^2). In the present analysis, the coordination number was kept fixed to the one extracted from diffraction data. For the EXAFS fitting analysis, the amplitude reduction factor, S_0^2, was extracted from EXAFS fitting of the Ni foil spectra and was fixed to the value of 0.8711 for all other samples. For each sample, we used up to 3–5 single and double scattering paths in the analysis extending beyond the next nearest-neighbor distance. In Table S6, more details on the EXAFS fitting for each compound can be found.

SUPPLEMENTAL INFORMATION

Supplemental information can be found online at https://doi.org/10.1016/j.xcrp.2023.101724.

ACKNOWLEDGMENTS

J.E.F.S.R. thanks Dr. Carlos Pecharroman and the Service of IR spectroscopy and ellipsometry of the "Instituto de Ciencia de Materiales de Madrid-CSIC" for FTIR measurements. The authors wish to express their gratitude to the ILL and the European Synchrotron Radiation Facility (ESRF) for making all facilities available for neutron and synchrotron diffraction experiments (ESRF proposal HC-4990 in ID22 and in-house beamtime in BM23). Electron microscopy observations were carried out at the Centro Nacional de Microscopia Electronica (CNME-UCM). We are thankful for funding from the Spanish Ministry of Science and Innovation (MCIN/AEI/10.13039/501100011033) with grant nos. PID2021-122477OB-I00, TED2021-129254B-C21, and TED2021-129254B-C22. J.G. thanks MCIN for

granting the contract PRE2018-083398. F.S.-S. is thankful for the grant RYC2021-033518-I, funded by NextGenerationEU and MICIN.

AUTHOR CONTRIBUTIONS

J.A.A. and J.L.M. conceived and designed the study. J.G. synthesized the samples. J.A.A., J.G., C.A.L., F.S.-S., and M.T.F.-D. carried out and analyzed the SXRD and NPD. J.L.M. and N.N.M. characterized the magnetic properties. N.B. performed and analyzed the transmission electron microscopy and EELS. J.E.F.S.R. and A.D.R. recorded and analyzed the XAS data. J.A.A. and N.N.M. coordinated the writing of the manuscript with discussion and input from all authors.

DECLARATION OF INTERESTS

The authors declare no competing interests.

Received: July 21, 2023
Revised: September 24, 2023
Accepted: November 13, 2023
Published: December 5, 2023

REFERENCES

1. Bednorz, J.G., and Müller, K.A. (1986). Possible high Tc superconductivity in the Ba-La-Cu-O system. Z. Physik B -. Condensed Matter *64*, 189–193.
2. Scalapino, D.J. (2012). A common thread: The pairing interaction for unconventional superconductors. Rev. Mod. Phys. *84*, 1383–1417.
3. Orenstein, J., and Millis, A.J. (2000). Advances in the Physics of High-Temperature Superconductivity. Science *288*, 468–475.
4. Anisimov, V.I., Bukhvalov, D., and Rice, T.M. (1999). Electronic structure of possible nickelate analogs to the cuprates. Phys. Rev. B *59*, 7901–7906.
5. Alonso, J.A., García-Muñoz, J.L., Fernández-Díaz, M.T., Aranda, M.A.G., Martínez-Lope, M.J., and Casais, M.T. (1999). Charge disproportionation in RNiO3 perovskites: Simultaneous metal-insulator and structural transition in YNiO3. Phys. Rev. Lett. *82*, 3871–3874.
6. Alonso, J.A., Martínez-Lope, M.J., Casais, M.T., Aranda, M.A.G., and Fernández-Díaz, M.T. (1999). Metal–Insulator Transitions, Structural and Microstructural Evolution of RNiO 3 (R = Sm, Eu, Gd, Dy, Ho, Y) Perovskites: Evidence for Room-Temperature Charge Disproportionation in Monoclinic HoNiO 3 and YNiO 3. J. Am. Chem. Soc. *121*, 4754–4762.
7. Alonso, J.A., Martínez-Lope, M.J., Casais, M.T., García-Muñoz, J.L., and Fernández-Díaz, M.T. (2000). Room-temperature monoclinic distortion due to charge disproportionation in RNiO3 perovskites with small rare-earth cations (R = Ho, Y, Er, Tm, Yb, and Lu): A neutron diffraction study. Phys. Rev. B *61*, 1756–1763.
8. Zhou, J.-S., and Goodenough, J.B. (2004). Chemical bonding and electronic structure of RNiO3 (R=rare earth). Phys. Rev. B *69*, 153105.
9. Li, B., Louca, D., Yano, S., Marshall, L.G., Zhou, J., and Goodenough, J.B. (2016). Insulating Pockets in Metallic LaNiO 3. Adv. Electron. Mater. *2*, 1500261.
10. Guo, H., Li, Z.W., Zhao, L., Hu, Z., Chang, C.F., Kuo, C.-Y., Schmidt, W., Piovano, A., Pi, T.W., Sobolev, O., et al. (2018). Antiferromagnetic correlations in the metallic strongly correlated transition metal oxide LaNiO3. Nat. Commun. *9*, 43.
11. Woolley, R.J., Illy, B.N., Ryan, M.P., and Skinner, S.J. (2011). In situ determination of the nickel oxidation state in La 2NiO4+δ and La4Ni3O 10-δ using X-ray absorption near-edge structure. J. Mater. Chem. *21*, 18592–18596.
12. Zhang, J., Botana, A.S., Freeland, J.W., Phelan, D., Zheng, H., Pardo, V., Norman, M.R., and Mitchell, J.F. (2017). Large orbital polarization in a metallic square-planar nickelate. Nat. Phys. *13*, 864–869.
13. Medarde, M.L. (1997). Structural, magnetic and electronic properties of RNiO3 perovskites (R = rare earth). J. Phys. Condens. Matter *9*, 1679–1707.
14. Catalan, G. (2008). Progress in perovskite nickelate research. Phase Transitions *81*, 729–749.
15. Fowlie, J., Gibert, M., Tieri, G., Gloter, A., Íñiguez, J., Filippetti, A., Catalano, S., Gariglio, S., Schober, A., Guennou, M., et al. (2017). Conductivity and Local Structure of LaNiO 3 Thin Films. Adv. Mater. *29*, 1605197.
16. Li, D., Lee, K., Wang, B.Y., Osada, M., Crossley, S., Lee, H.R., Cui, Y., Hikita, Y., and Hwang, H.Y. (2019). Superconductivity in an infinite-layer nickelate. Nature *572*, 624–627.
17. Li, D., Wang, B.Y., Lee, K., Harvey, S.P., Osada, M., Goodge, B.H., Kourkoutis, L.F., and Hwang, H.Y. (2020). Superconducting Dome in Nd1-xSrxNiO2 Infinite Layer Films. Phys. Rev. Lett. *125*, 027001.
18. Zeng, S., Tang, C.S., Yin, X., Li, C., Li, M., Huang, Z., Hu, J., Liu, W., Omar, G.J., Jani, H., et al. (2020). Phase Diagram and Superconducting Dome of Infinite-Layer Nd1-xSrxNiO2 Thin Films. Phys. Rev. Lett. *125*, 147003.
19. Osada, M., Wang, B.Y., Lee, K., Li, D., and Hwang, H.Y. (2020). Phase diagram of infinite layer praseodymium nickelate Pr1-xSrxNiO2 thin films. Phys. Rev. Mater. *4*, 121801.
20. Osada, M., Wang, B.Y., Goodge, B.H., Lee, K., Yoon, H., Sakuma, K., Li, D., Miura, M., Kourkoutis, L.F., and Hwang, H.Y. (2020). A Superconducting Praseodymium Nickelate with Infinite Layer Structure. Nano Lett. *20*, 5735–5740.
21. Osada, M., Wang, B.Y., Goodge, B.H., Harvey, S.P., Lee, K., Li, D., Kourkoutis, L.F., and Hwang, H.Y. (2021). Nickelate Superconductivity without Rare-Earth Magnetism: (La,Sr)NiO2. Adv. Mater. *33*, 2104083.
22. Zeng, S., Li, C., Chow, L.E., Cao, Y., Zhang, Z., Tang, C.S., Yin, X., Lim, Z.S., Hu, J., Yang, P., and Ariando, A. (2022). Superconductivity in infinite-layer nickelate La 1−x Ca x NiO 2 thin films. Sci. Adv. *8*, 9927.
23. Pan, G.A., Ferenc Segedin, D., LaBollita, H., Song, Q., Nica, E.M., Goodge, B.H., Pierce, A.T., Doyle, S., Novakov, S., Córdova Carrizales, D., et al. (2022). Superconductivity in a quintuple-layer square-planar nickelate. Nat. Mater. *21*, 160–164.
24. Lee, K.-W., and Pickett, W.E. (2004). Infinite-layer LaNiO2: Ni1+ is not Cu2+. Phys. Rev. B *70*, 165109.
25. Ji, Y., Liu, J., Li, L., and Liao, Z. (2021). Superconductivity in infinite layer nickelates. J. Appl. Phys. *130*, 060901.
26. Mitchell, J.F. (2021). A Nickelate Renaissance. Front. Phys. *9*, 1–8.

27. Kitatani, M., Si, L., Janson, O., Arita, R., Zhong, Z., and Held, K. (2020). Nickelate superconductors—a renaissance of the one-band Hubbard model. NPJ Quantum Mater. *5*. 59–11.

28. Zhang, G.M., Yang, Y.F., and Zhang, F.C. (2020). Self-doped Mott insulator for parent compounds of nickelate superconductors. Phys. Rev. B *101*, 20501–20505.

29. Been, E., Lee, W.-S., Hwang, H.Y., Cui, Y., Zaanen, J., Devereaux, T., Moritz, B., and Jia, C. (2021). Electronic Structure Trends Across the Rare-Earth Series in Superconducting Infinite-Layer Nickelates. Phys. Rev. X *11*, 011050.

30. Kang, B., Kim, H., Zhu, Q., and Park, C.H. (2023). Impact of f-d Kondo cloud on superconductivity of nickelates. Cell Rep. Phys. Sci. *4*, 101325.

31. Hepting, M., Li, D., Jia, C.J., Lu, H., Paris, E., Tseng, Y., Feng, X., Osada, M., Been, E., Hikita, Y., et al. (2020). Electronic structure of the parent compound of superconducting infinite-layer nickelates. Nat. Mater. *19*, 381–385.

32. Ortiz, R.A., Puphal, P., Klett, M., Hotz, F., Kremer, R.K., Trepka, H., Hemmida, M., von Nidda, H.-A.K., Isobe, M., Khasanov, R., et al. (2022). Magnetic correlations in infinite-layer nickelates: An experimental and theoretical multimethod study. Phys. Rev. Res. *4*, 023093.

33. Wang, N.N., Yang, M.W., Yang, Z., Chen, K.Y., Zhang, H., Zhang, Q.H., Zhu, Z.H., Uwatoko, Y., Gu, L., Dong, X.L., et al. (2022). Pressure-induced monotonic enhancement of Tc to over 30 K in superconducting Pr0.82Sr0.18NiO2 thin films. Nat. Commun. *13*, 4367.

34. Lu, H., Rossi, M., Nag, A., Osada, M., Li, D.F., Lee, K., Wang, B.Y., Garcia-Fernandez, M., Agrestini, S., Shen, Z.X., et al. (2021). Magnetic excitations in infinite-layer nickelates. Science (80-.) *373*, 213–216.

35. Tam, C.C., Choi, J., Ding, X., Agrestini, S., Nag, A., Wu, M., Huang, B., Luo, H., Gao, P., García-Fernández, M., et al. (2022). Charge density waves in infinite-layer NdNiO2 nickelates. Nat. Mater. *21*, 1116–1120.

36. Rossi, M., Osada, M., Choi, J., Agrestini, S., Jost, D., Lee, Y., Lu, H., Wang, B.Y., Lee, K., Nag, A., et al. (2022). A broken translational symmetry state in an infinite-layer nickelate. Nat. Phys. *18*, 869–873.

37. Li, Y., Li, Z., Li, Q., Tian, M., Li, C., Sun, L., Wang, J., Zhao, X., Xu, S., and Yu, F. (2020). Absence of superconductivity in bulk Nd1−xSrxNiO2. Commun. Mater. *15*, 16.

38. Si, L., Xiao, W., Kaufmann, J., Tomczak, J.M., Lu, Y., Zhong, Z., and Held, K. (2020). Topotactic Hydrogen in Nickelate Superconductors and Akin Infinite-Layer Oxides AB O2. Phys. Rev. Lett. *124*, 166402–166408.

39. Malyi, O.I., Varignon, J., and Zunger, A. (2022). Bulk NdNiO2 is thermodynamically unstable with respect to decomposition while hydrogenation reduces the instability and transforms it from metal to insulator. Phys. Rev. B *105*, 014106.

40. Puphal, P., Pomjakushin, V., Ortiz, R.A., Hammoud, S., Isobe, M., Keimer, B., and Hepting, M. (2022). Investigation of Hydrogen Incorporations in Bulk Infinite-Layer Nickelates. Front. Phys. *10*, 1–6.

41. Si, L., Worm, P., and Held, K. (2022). Fingerprints of Topotactic Hydrogen in Nickelate Superconductors. Crystals *12*, 656.

42. Ding, X., Tam, C.C., Sui, X., Zhao, Y., Xu, M., Choi, J., Leng, H., Zhang, J., Wu, M., Xiao, H., et al. (2023). Critical role of hydrogen for superconductivity in nickelates. Nature *615*, 50–55.

43. Takamatsu, T., Kato, M., Noji, T., and Koike, Y. (2010). Low-temperature synthesis of the infinite-layer compound LaNiO2 using CaH2 as reductant. Phys. C Supercond. its Appl. *470*, S764–S765.

44. Hayward, M.A., Green, M.A., Rosseinsky, M.J., and Sloan, J. (1999). Sodium Hydride as a Powerful Reducing Agent for Topotactic Oxide Deintercalation: Synthesis and Characterization of the Nickel(I) Oxide LaNiO 2. J. Am. Chem. Soc. *121*, 8843–8854.

45. Hayward, M.A., and Rosseinsky, M.J. (2003). Synthesis of the infinite layer Ni(I) phase NdNiO2+x by low temperature reduction of NdNiO3 with sodium hydride. Solid State Sci. *5*, 839–850.

46. Wang, B.-X., Zheng, H., Krivyakina, E., Chmaissem, O., Lopes, P.P., Lynn, J.W., Gallington, L.C., Ren, Y., Rosenkranz, S., Mitchell, J.F., and Phelan, D. (2020). Synthesis and characterization of bulk Nd1-xSrxNiO2 and Nd1-xSrxNiO3. Phys. Rev. Mater. *4*, 084409.

47. He, C., Ming, X., Li, Q., Zhu, X., Si, J., and Wen, H.-H. (2021). Synthesis and physical properties of perovskite Sm 1−x Sr x NiO 3 (x = 0, 0.2) and infinite-layer Sm 0.8 Sr 0.2 NiO 2 nickelates. J. Phys. Condens. Matter *33*, 265701.

48. Martínez-Lope, M., Casais, M., and Alonso, J. (1998). Stabilization of Ni+ in defect perovskites La(Ni1−xAlx)O2+x with 'infinite-layer' structure. J. Alloys Compd. *275–277*, 109–112.

49. Cui, Y., Li, C., Li, Q., Zhu, X., Hu, Z., Yang, Y.f., Zhang, J., Yu, R., Wen, H.-H., and Yu, W. (2021). NMR evidence of antiferromagnetic spin fluctuations in Nd0. 85Sr0. 15NiO2. Chinese Phys. Lett. *38*, 067401.

50. Bernardini, F., Bosin, A., and Cano, A. (2022). Geometric effects in the infinite-layer nickelates. Phys. Rev. Mater. *6*, 044807.

51. Si, L., Worm, P., Chen, D., and Held, K. (2023). Topotactic hydrogen forms chains in ABO2 nickelate superconductors. Phys. Rev. B *107*, 165116.

52. Puphal, P., Wu, Y.-M., Fürsich, K., Lee, H., Pakdaman, M., Bruin, J.A.N., Nuss, J., Suyolcu, Y.E., van Aken, P.A., Keimer, B., et al. (2021). Topotactic transformation of single crystals: From perovskite to infinite-layer nickelates. Sci. Adv. *7*, 1–10.

53. Leapman, R.D., Grunes, L.A., and Fejes, P.L. (1982). Study of the L 23 edges in the 3 d transition metals and their oxides by electron-energy-loss spectroscopy with comparisons to theory. Phys. Rev. B *26*, 614–635.

54. Abbate, M., De Groot, F.M.F., Fuggle, J.C., Fujimori, A., Tokura, Y., Fujishima, Y., Strebel, O., Domke, M., Kaindl, G., Van Elp, J., et al. (1991). Soft-x-ray-absorption studies of the location of extra charges induced by substitution in controlled-valence materials. Phys. Rev. B *44*, 5419–5422.

55. Botton, G.A., Appel, C.C., Horsewell, A., and Stobbs, W.M. (1995). Quantification of the EELS near-edge structures to study Mn doping in oxides. J. Microsc. *180*, 211–216.

56. Krstulović, M., Rosa, A.D., Biedermann, N., Irifune, T., and Wilke, M. (2021). Structural changes in aluminosilicate glasses up to 164 GPa and the role of alkali, alkaline earth cations and alumina in the densification mechanism. Chem. Geol. *560*, 119980.

57. Siegrist, T., Zahurak, S.M., Murphy, D.W., and Roth, R.S. (1988). The parent structure of the layered high-temperature superconductors. Nature *334*, 231–232.

58. Crespin, M., Levitz, P., and Gatineau, L. (1983). Reduced forms of LaNiO 3 perovskite. Part 1.—Evidence for new phases: La 2 Ni 2 O 5 and LaNiO 2. J. Chem. Soc., Faraday Trans. 2 *79*, 1181–1194. 2.

59. Si, L., Worm, P., Chen, D., and Held, K. (2023). Topotactic hydrogen forms chains in A B O 2 nickelate superconductors. Phys. Rev. B *107*, 165116.

60. Fitch, A., and Dejoie, C. (2021). Combining a multi-analyzer stage with a two-dimensional detector for high-resolution powder X-ray diffraction: correcting the angular scale. J. Appl. Crystallogr. *54*, 1088–1099.

61. Fitch, A., Dejoie, C., Covacci, E., Confalonieri, G., Grendal, O., Claustre, L., Guillou, P., Kieffer, J., de Nolf, W., Petitdemange, S., et al. (2023). ID22 – the high-resolution powder-diffraction beamline at ESRF. J. Synchrotron Radiat. *30*, 1003–1012.

62. Rietveld, H.M. (1969). A profile refinement method for nuclear and magnetic structures. J. Appl. Crystallogr. *2*, 65–71.

63. Rodríguez-Carvajal, J. (1993). Recent advances in magnetic structure determination by neutron powder diffraction. Phys. B Phys. Condens. Matter *192*, 55–69.

64. Mathon, O., Beteva, A., Borrel, J., Bugnazet, D., Gatla, S., Hino, R., Kantor, I., Mairs, T., Munoz, M., Pasternak, S., et al. (2015). The time-resolved and extreme conditions XAS (Texas) facility at the European Synchrotron Radiation Facility: The general-purpose EXAFS bending-magnet beamline BM23. J. Synchrotron Radiat. *22*, 1548–1554.

65. da Costa, R.C., Rodrigues, J.E., Gualdi, A.J., Cunha, T.R., Rodrigues, A.D., Marques, P.W., Hernandes, A.C., and Pizani, P.S. (2018). Dielectric and Magnetic Properties of NixPb1-xTiO3 Solid Solution and Composite: Coexistence of Ferroelectric and Antiferromagnetic Order. J. Alloys Compd. *739*, 600–606.

66. Ravel, B., and Newville, M. (2005). ATHENA , ARTEMIS , HEPHAESTUS : data analysis for X-ray absorption spectroscopy using IFEFFIT. J. Synchrotron Radiat. *12*, 537–541.